Research Article

# Quasi-Type II Core−Shell Perovskite Nanocrystals for Improved Structural Stability and Optical Gain

Xuanyu Zhang, Zhihang Guo, Ruxue Li, Jiahao Yu, Baozhen Yuan, Baian Chen, Tingchao He,* and Rui Chen*

Cite This: *ACS Appl. Mater. Interfaces* 2021, 13, 58170−58178

Read Online

ACCESS | 📊 Metrics & More | 📖 Article Recommendations | 🆂🅸 Supporting Information

**ABSTRACT:** In recent years, core−shell lead halide perovskite nanocrystals (PeNCs) and their devices have attracted intensive attention owing to nearly perfect optoelectronic properties. However, the complex photophysical mechanism among them is still unclear. Herein, monodispersed core−shell PeNCs coated with an all-inorganic cesium lead bromide ($CsPbBr_3$) shell epitaxially grown on the surface of formamidinium lead bromide ($FAPbBr_3$) PeNCs were synthesized. Through power- and temperature-dependent photoluminescence (PL) measurements, it is found that the electronic structure of the core−shell $FAPbBr_3/CsPbBr_3$ PeNCs has a quasi-type II band alignment. The presence of $Cs^+$ in the shell limits ion migration and helps to stabilize structural and optical properties. On this basis, after being exposed to pulsed nanosecond laser for a period, an amplified spontaneous emission (ASE) can be observed, which is attributed to the effective passivation induced by laser irradiation on defects at the interface. The ASE threshold of the core−shell PeNCs showing high structural and optical stability is 447 $nJ/cm^2$ under pulsed nanosecond optical pumping. The results that are demonstrated here provide a new idea and perspective for improving the stability of perovskite and can be of practical interest for the utilization of the core−shell PeNCs in optoelectronic devices.

**KEYWORDS:** *core−shell perovskite nanocrystals, quasi-type II band alignment, laser spectroscopy, photostability, amplified spontaneous emission*
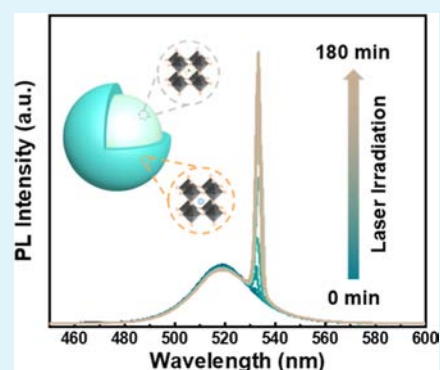
## INTRODUCTION

Lead halide perovskite nanocrystals (PeNCs) have become a promising candidate in the field of optoelectronics owing to their large optical absorption coefficient ($10^4-10^5$ $cm^{-1}$), tunable band gap, narrow emission bandwidth, and high photoluminescence quantum yield (PLQY).[1−5] The power conversion efficiency (PCE) of the monolithic perovskite/silicon tandem solar cell has already reached 29.15% within a very short period.[6] Meanwhile, multicolor light-emitting diodes (LEDs) and low threshold optical-pumped lasers have been realized with excellent performance.[7,8] However, the ionic nature of PeNCs results in a significant drawback of high environmental sensitivity, which limits their practical applications.[9,10] Furthermore, up to now, studies have shown that high-temperature, oxygen, moisture, ultraviolet (UV) light exposure, and structural transformation lead to the decomposition of perovskite materials and degrade the device stability.[11−15] Therefore, progress in improving the stability of the material without sacrificing its performance is crucial for the development of PeNCs in the future.

Recent studies have been carried out for obtaining stable and high-performance perovskite materials by developing synthesis methods and post-treatments, such as doping, underlayer abduction, and additive additions.[16,17] Among them, the most effective approach is to cover other materials around PeNCs.[18−20] Researchers developed a facial method for coating a $TiO_2$ shell on PeNCs, greatly improving their stability.[21] The resulting $CsPbBr_3/TiO_2$ core−shell structures are ultrastable and exhibit excellent water stability of more than 12 weeks. The size, morphology, and crystallinity remained unchanged, which could provide additional protection against anion exchange and photodegradation. We encapsulated $MAPbBr_3$ microcrystals in a very dense $Al_2O_3$ layer by the atomic layer deposition. It was found that the self-structural healing phenomenon took place after thermal heating or laser irradiation. More importantly, the density of deep level trap states was greatly reduced, which resulted in high thermal stability and excellent lasing stability of up to 2 years.[19] However, the presence of an oxide layer outside the PeNCs prevents efficient current injection required for applications such as LEDs and solar cells. Meanwhile, the covering of an

oxide layer requires complicated processes, such as high-temperature sintering. Therefore, the use of a semiconductor heterostructure, especially other perovskite materials as a shell, not only ensures the stability of the core but also enables current injection. In 2016, a core−shell mixed three-dimensional methylammonium (MA)−two-dimensional octylammonium (OA) lead bromide perovskite was fabricated, which realized high stability and tunable colors.[22] Subsequently, giant five-photon absorption was achieved in this new family of PeNCs, which is promising for developing the next-generation multiphoton imaging with unmatched imaging depth, sensitivity, and resolution.[23] Although the core−shell MAPbBr$_3$/(OA)$_2$PbBr$_4$ possesses amazing optical properties, the large lattice mismatch between two materials induces the formation of defect or trap states at the interface, which plagues the development of their applications.[24,25]

Compared with various traditional perovskite materials such as MAPbBr$_3$ and CsPbBr$_3$, FAPbBr$_3$ PeNCs have drawn intensive research attention recently due to their ultrapure green emission that covers ≈95% Rec. 2020 standard in the CIE 1931 color space.[26] Meanwhile, LEDs based on FAPbBr$_3$ PeNCs were fabricated with high efficiency and long lifetime.[27] It is noted that the lattice mismatch between FAPbBr$_3$ and CsPbBr$_3$ is 3.4%,[28] which is much smaller than that of MAPbBr$_3$/(OA)$_2$PbBr$_4$ mentioned above. It is known that the electronic structure of the core−shell material induces unique physical properties. However, no detailed investigation on the photophysical process of such materials has been carried out.

Therefore, in this work, core−shell FAPbBr$_3$/CsPbBr$_3$ PeNCs were fabricated via heteroepitaxial methods. The electronic structure of the quasi-type II band alignment in core−shell FAPbBr$_3$/CsPbBr$_3$ PeNCs was studied through temperature- and power-dependent photoluminescence (PL). In addition, both the core-only FAPbBr$_3$ and the core−shell FAPbBr$_3$/CsPbBr$_3$ PeNCs were exposed to nanosecond laser irradiation. The smaller emission attenuation and peak shifting of the core−shell FAPbBr$_3$/CsPbBr$_3$ PeNCs reveal their better stability. Moreover, it is interesting to observe the amplified spontaneous emission (ASE) from the core−shell PeNCs with a threshold of 447 nJ/cm$^2$, which can be attributed to the surface defect passivation due to laser irradiation. The results demonstrated here offer realistic prospects for the utilization of the core−shell PeNCs for optoelectronics.

## ■ EXPERIMENTAL SECTION

**Synthesis of Perovskite Nanocrystals.** FAPbBr$_3$ PeNCs were synthesized according to the method reported previously.[23] All reagents were purchased and used without further purification, including FA-acetate (Sigma-Aldrich), Pb(CH$_3$COO)$_2$·3H$_2$O (Sinopharm Chemical Reagent Co., Ltd., ≥99.5%), octadecene (ODE, Sigma-Aldrich, 90%), OA (Sigma-Aldrich, 90%), OAmBr (Xi'an Polymer Light Technology Corp.), toluene (Sinopharm Chemical Reagent Co., Ltd., ≥99.5%), PbBr$_2$ (Sigma-Aldrich, 90%), Cs$_2$CO$_3$ (Sigma-Aldrich), and OLA (Sigma-Aldrich, 90%). Briefly, FA-acetate (0.078 g, 0.75 mmol), Pb(CH$_3$COO)$_2$·3H$_2$O (0.076 g, 0.2 mmol), OA (2 mL, vacuum-dried at 120 °C), and ODE (8 mL, vacuum-dried at 120 °C) were loaded into a 100 mL flask and dried for 30 min under vacuum at 50 °C. The mixture was heated to 130 °C under an N$_2$ atmosphere and OAmBr (0.21 g, 0.6 mmol) in toluene (2 mL) was injected. After 10 s, the reaction mixture was cooled on an ice-water bath. The green solution of FAPbBr$_3$ PeNCs was collected and stored at 4 °C.

For the synthesis of the core−shell FAPbBr$_3$/CsPbBr$_3$ PeNCs, PbBr$_2$ (0.1101 g, 0.3 mmol) and Cs$_2$CO$_3$ (0.0326 g, 0.1 mmol) were loaded into a 100 mL flask. Then, dried OA (1 mL), ODE (5 mL),

OLA (0.5 mL), and the as-synthesized FAPbBr$_3$ PeNCs (12 mL) were added. The mixture was heated to 80 °C for 20 min under an N$_2$ atmosphere, followed by cooling on an ice bath. The color of the reaction solution varied significantly compared to the original solution of FAPbBr$_3$ PeNCs. Finally, the solution was centrifuged to remove undispersed residue and aggregated PeNCs. The core−shell FAPbBr$_3$/CsPbBr$_3$ PeNCs were dispersed in hexane and stored in the dark at 4 °C.

**Purification.** The as-prepared crude solutions of FAPbBr$_3$ and core−shell FAPbBr$_3$/CsPbBr$_3$ PeNCs were loaded into centrifuge tubes, a certain volume of ethyl acetate was added (keeping the volume ratio of crude solution to ethyl acetate 1:3), and the mixture was centrifuged at 7000 rpm for 5 min. The precipitate was then redissolved in *n*-hexane and centrifuged for 1 min at 5000 rpm. After that, the supernatant was collected and stored at 4 °C. Finally, after washing twice or three times, the purified perovskite PeNC solution was obtained.

**Characterization Methods.** The samples for transmission electron microscopy (TEM) measurements were prepared by dropping colloidal PeNC solution with a relatively dilute concentration on carbon-coated 200 mesh copper grids. Also, the conventional TEM image and energy-dispersive spectrometry (EDS) were achieved by a Talos F200X microscope equipped with a thermionic gun under an acceleration voltage of 200 kV. The current of the 1 nm electron beam at this voltage is 1.5 nA, and the resolution is 0.12 nm. UV−vis absorption spectra were recorded at room temperature on an ultraviolet and visible spectrophotometer (Lambda 950, PerkinElmer, Inc.). All PL spectra were recorded by a spectrometer (Andor SR-750) and detected using a charge-coupled device (CCD, model No. DU920P-BU). A continuous-wave (CW) He−Cd gas laser with a laser line of 325 nm was used as the excitation source for power- and temperature-dependent PL measurements. FAPbBr$_3$ and the core−shell FAPbBr$_3$/CsPbBr$_3$ PeNCs films were placed inside a closed-cycle helium cryostat (Cryo Industries of America) with quartz windows for temperature-dependent PL measurements, and the temperature of the sample was controlled by a commercial temperature controller (Lakeshore 336). The temperature during the PL measurement is well-controlled from 50 to 295 K. For the power-dependent PL measurement, a variable neutral density filter was used to obtain different excitation powers. A pulsed 355 nm laser with a pulse width of 1 ns and frequency of 20 Hz was employed for optical pumping. The micro-PL experiment was performed by inverted optical microscopy (Nikon Ti-u). Time-resolved photoluminescence (TRPL) experiments were carried out at room temperature and the excitation source was a pulsed ultraviolet picosecond diode laser operating at 375 nm. The pulse width and repetition rate of the laser were 40 ps and 20 MHz, respectively. The signal was dispersed by a 320 mm monochromator (iHR320 from Horiba, Ltd.) combined with suitable filters and detected based on the time-correlated single-photon counting (TCSPC) technique. For the microwave treatment, the core−shell FAPbBr$_3$/CsPbBr$_3$ PeNCs films were placed inside the microwave oven (DAEWOO, KOR-4A6BR) with the maximum output power (500 W) for 0, 3, and 5 min, respectively. To ensure comparability of emission, optical alignment is fixed during the measurement.

**Computational Method.** The density functional theory (DFT) was applied in this work using the CASTEP module[29] in Materials Studio software to calculate the band structures and work functions of the orthorhombic phase CsPbBr$_3$ and cubic phase FAPbBr$_3$. The models of cubic and orthorhombic CsPbBr$_3$ were downloaded from the Materials Project database[30] where available, and the cubic FAPbBr$_3$ was generated by the substitution between the cation CH(NH$_2$)$_2$$^+$ (FA$^+$) and the primary cation Cs$^+$. The generalized gradient approximation (GGA) with the Perdew−Burke−Ernzerhof (PBE) functional[31] was chosen to treat the exchange-correlation terms. Self-consistent iterations with density-mixing were implemented to obtain the electronic wave functions and the Broyden−Fletcher−Goldfarb−Shannon (BFGS) algorithm[32] was used to realize the structure relaxation. During the process of the geometry optimization, the plane waves cutoff energy was set as 244.9 eV for
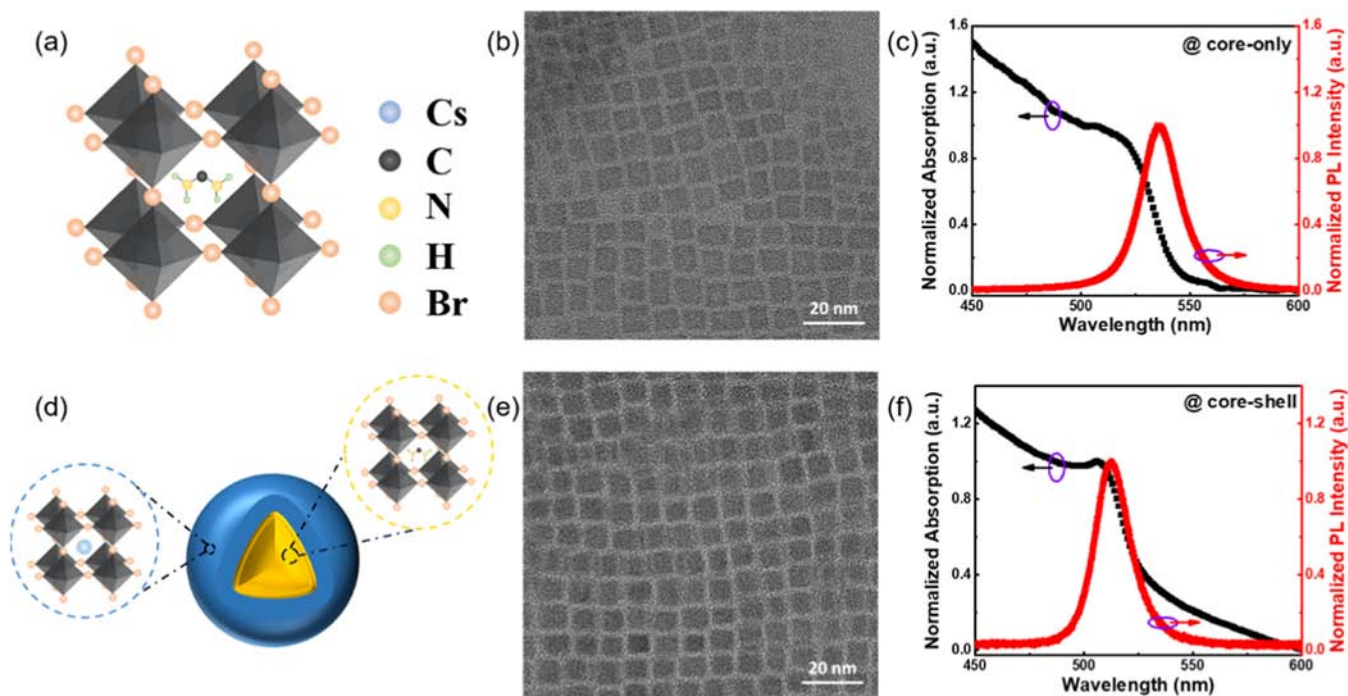
**Figure 1.** (a, d) Schematic structure of FAPbBr$_3$ and the core−shell FAPbBr$_3$/CsPbBr$_3$ PeNCs, respectively. (b, e) TEM images of FAPbBr$_3$ and the core−shell FAPbBr$_3$/CsPbBr$_3$ PeNCs, respectively. (c, f) Absorption (black curve) and photoluminescence (red curve) spectra at room temperature, respectively.
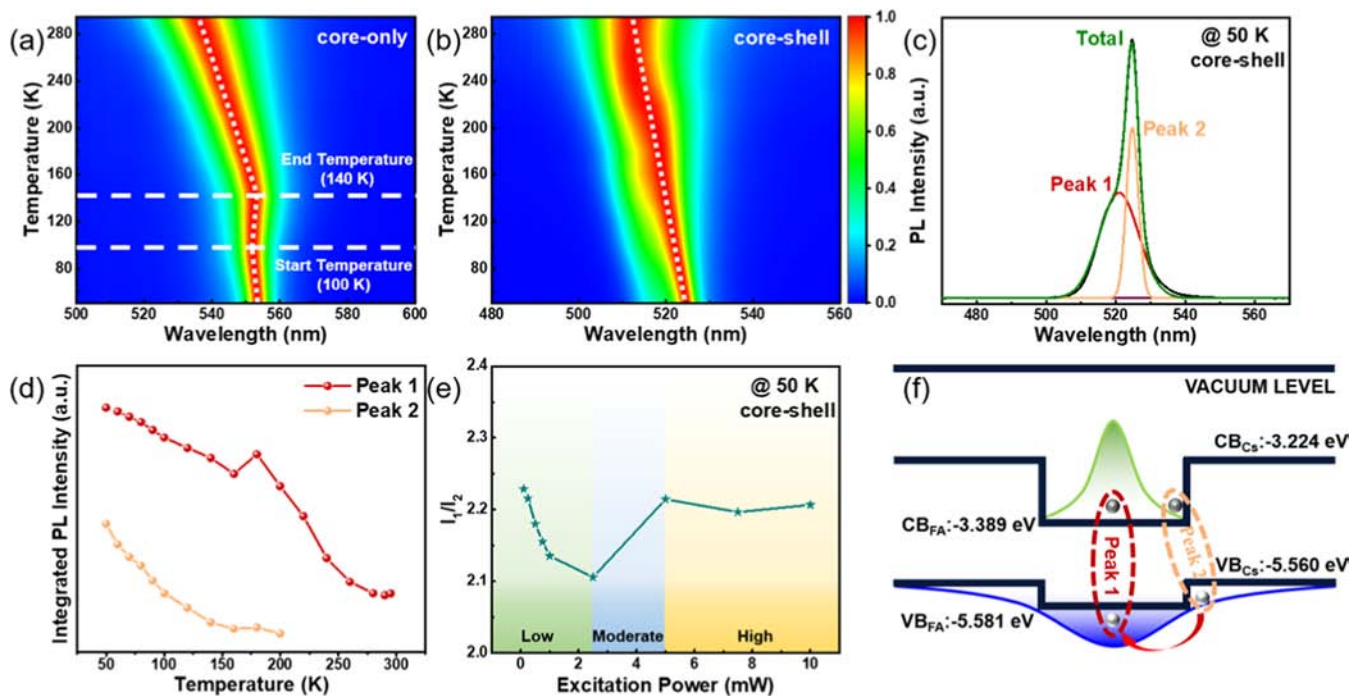


**Figure 2.** Normalized PL spectra of a 2D pseudocolor plot of FAPbBr$_3$ (a) and core/shell FAPbBr$_3$/CsPbBr$_3$ (b) PeNCs at temperature between 50 and 295 K. (c) Emission spectrum from the core−shell FAPbBr$_3$/CsPbBr$_3$ PeNCs at 50 K. (d) Integrated PL intensity of the core−shell FAPbBr$_3$/CsPbBr$_3$ PeNCs as a function of temperature. (e) Emission intensity ratio of Peak 1 to Peak 2 at 50 K under different excitation intensities. (f) Proposed quasi-type II energy structure of the core−shell FAPbBr$_3$/CsPbBr$_3$ PeNCs.

orthorhombic CsPbBr$_3$ and 435.4 eV for cubic FAPbBr$_3$, and the Monkhorst−Pack grid[33] parameters over the Brillouin zone were set as $1 \times 1 \times 1$ for orthorhombic CsPbBr$_3$ and $2 \times 2 \times 2$ for cubic FAPbBr$_3$, respectively. The convergence tolerance parameters were uniformly set as energy tolerance $2 \times 10^{-5}$ eV/atom, force tolerance $5 \times 10^{-2}$ eV/Å, stress tolerance 0.1 GPa, and maximum displacement 2 $\times 10^{-3}$ Å. The band structures of these materials were calculated by applying the ultrasoft pseudopotential and the Monkhorst−Pack grid parameters were set as $2 \times 2 \times 2$ for orthorhombic CsPbBr$_3$ and $4 \times 4 \times 4$ for cubic FAPbBr$_3$, respectively. The (011) plane of orthorhombic CsPbBr$_3$ and the (010) plane of cubic FAPbBr$_3$ were purposely selected and cleaved to further test the corresponding work
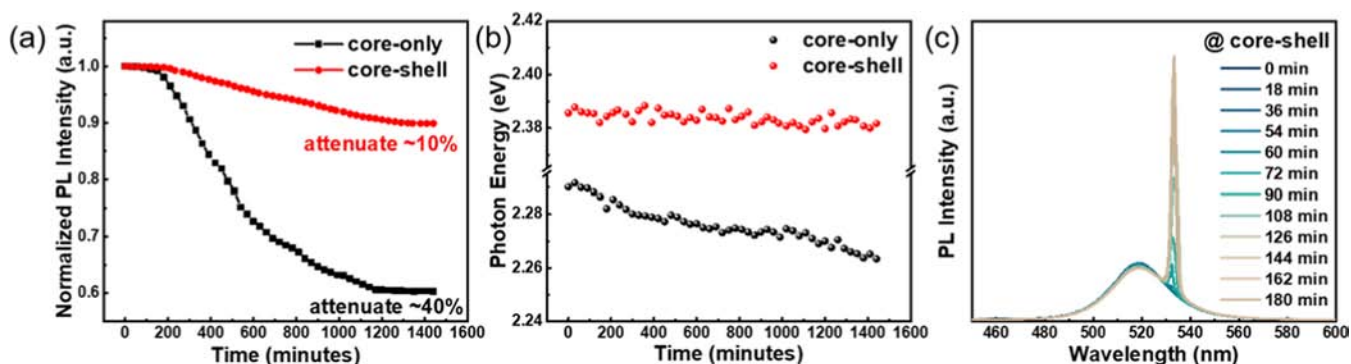
**Figure 3.** Monitoring of PL intensity (a) and photon energy (b) of FAPbBr$_3$ and core−shell FAPbBr$_3$/CsPbBr$_3$ PeNCs within time. (c) Emissions from the core−shell FAPbBr$_3$/CsPbBr$_3$ PeNCs under excitation density of 1500 $\mu$J cm$^{-2}$ as a function of time.

function properties. The final computed results were found to be highly consistent with the experimental data.

## RESULTS AND DISCUSSION

The schematic structures of colloidal FAPbBr$_3$ and core−shell FAPbBr$_3$/CsPbBr$_3$ PeNCs are drawn in Figure 1a,d, respectively. Representative TEM characterizations are shown in Figure 1b,e, which indicate that both samples retain cubic shape with an average size of 6.0 ± 1.2 and 9.0 ± 1.2 nm, respectively. Figure 1c,f shows the normalized UV−vis absorption and the PL emission spectra of FAPbBr$_3$ and core−shell FAPbBr$_3$/CsPbBr$_3$ PeNCs, respectively. It can be seen clearly that the absorption band edge of FAPbBr$_3$ PeNCs is located at 516 nm, while the emission centered at 536 nm with a full wavelength at half maximum (FWHM) of 21 nm. In comparison, the core−shell FAPbBr$_3$/CsPbBr$_3$ PeNCs exhibit a clear excitonic absorption peak at 506 nm, which implies the bigger exciton binding energy, and the emission shifts to 513 nm with an FWHM of 20 nm. The blue-shift of the emission from the core−shell PeNCs can be attributed to the reduced effective size of the FAPbBr$_3$ core due to the formation of the FA$_x$Cs$_{1-x}$PbBr$_3$ alloyed layer during the growth of the shell.[34]

Figure 2a,b show the normalized temperature-dependent PL mapping of FAPbBr$_3$ and core−shell FAPbBr$_3$/CsPbBr$_3$ PeNCs, respectively. It can be clearly seen in Figure 2a that the emission peak of FAPbBr$_3$ PeNCs does not change significantly with temperatures below 100 K. However, a red-shift of the emission peak was observed from 100 to 140 K (Figure S1). According to previous reports,[35,36] the structural phase transition from orthorhombic to tetragonal should be accounted for this red-shift in FAPbBr$_3$ PeNCs. Moreover, theoretical calculations show that the tetragonal phase has a smaller band gap than the orthorhombic phase,[37] which also supports this observation. It is noted that the phase transition temperature is lower than that in previous research works,[35,36] which may be due to the smaller size of the PeNCs.[38,39] The blue-shift of emission with temperature from 140 to 295 K can be described by the temperature coefficient $\alpha = \partial E_g / \partial T = 0.359$ meV/K. This is mainly attributed to the thermal expansion (TE) of lattice due to the anharmonicity of the interatomic potentials.[40,41] In comparison, the PL peak position of the core−shell FAPbBr$_3$/CsPbBr$_3$ PeNCs follows a continuous blue-shift from 50 to 295 K, which suggests that no phase transition takes place during this temperature range, likely due to the internal strain or a built-in electric field.[42,43] Moreover, negative thermal quenching only exists in FAPbBr$_3$ PeNCs as shown in Figure S1c,f, which implies more surface

defect states of the material.[40] It is worth noting that the emission from the core−shell PeNCs possesses two peaks at low temperature (50 K) as shown in Figure 2c, namely, Peak 1 and Peak 2, respectively, which can be distinguished from the Gaussian fitting ($R^2 = 0.999$). Peak 1 is located at 520.9 nm (2.38 eV) and the sharp Peak 2 is at 524.8 nm (2.36 eV). However, only Peak 1 can be observed at room temperature. There are several possibilities for the origin of the low-energy emission (Peak 2), such as biexcitons, defect states, bound excitons, and reabsorption. The physical mechanism of this observation will be discussed later based on the position and intensity relationship between the two emissions at low temperatures.

The integrated PL intensities of the two emissions at different temperatures were extracted and are plotted in Figure 2d. With the increase in temperature, the integrated PL intensity of Peak 2 decreases and vanishes around 200 K. On the other hand, the intensity of Peak 1 decreases first and then increases when the temperature reaches 180 K. Hereafter, Peak 1 dominates the emission above 200 K, and the integrated PL intensity decreases significantly with temperature. To further determine the origin of the two emissions, power-dependent PL measurement at low temperature (50 K) was performed, and the PL spectra under different excitation powers (0.10− 10.00 mW) are shown in Figure S3. The integrated PL intensity of Peaks 1 and 2 are both proportional to the excitation power, which can be well-described by the power-law function $I_{PL} \propto I_{ex}^k$.[44] The slope ($k$) of the two emissions can be determined to be 1.12 and 1.10 as shown in Figure S3b, implying that both emissions come from excitonic recombination. It is known that the integrated intensity of biexciton emission is usually proportional to the square of the excitation power.[45] Moreover, the energy separation between the exciton absorption peak and Peak 2 is around 90 meV, which is bigger than the biexciton binding energy (ranging from 1/10 to 1/5 of the exciton binding energy).[46,47] Furthermore, the integrated PL intensity of Peak 2 does not saturate with the increase of the excitation power. Therefore, the possibility that Peak 2 originates from the biexciton emission or defect states can be ruled out. The emission intensity ratio of Peak 1 and Peak 2 ($I_1/I_2$) is extracted and shown in Figure 2e. With the increase of excitation power, this ratio first decreases and then increases, and finally becomes identical, which indicates that Peak 2 is not related to bound exciton emission.

Based on the above discussion, it can be concluded that Peak 1 and Peak 2 emissions both originate from free exciton (FE) recombination. Taking into account the electron affinity and
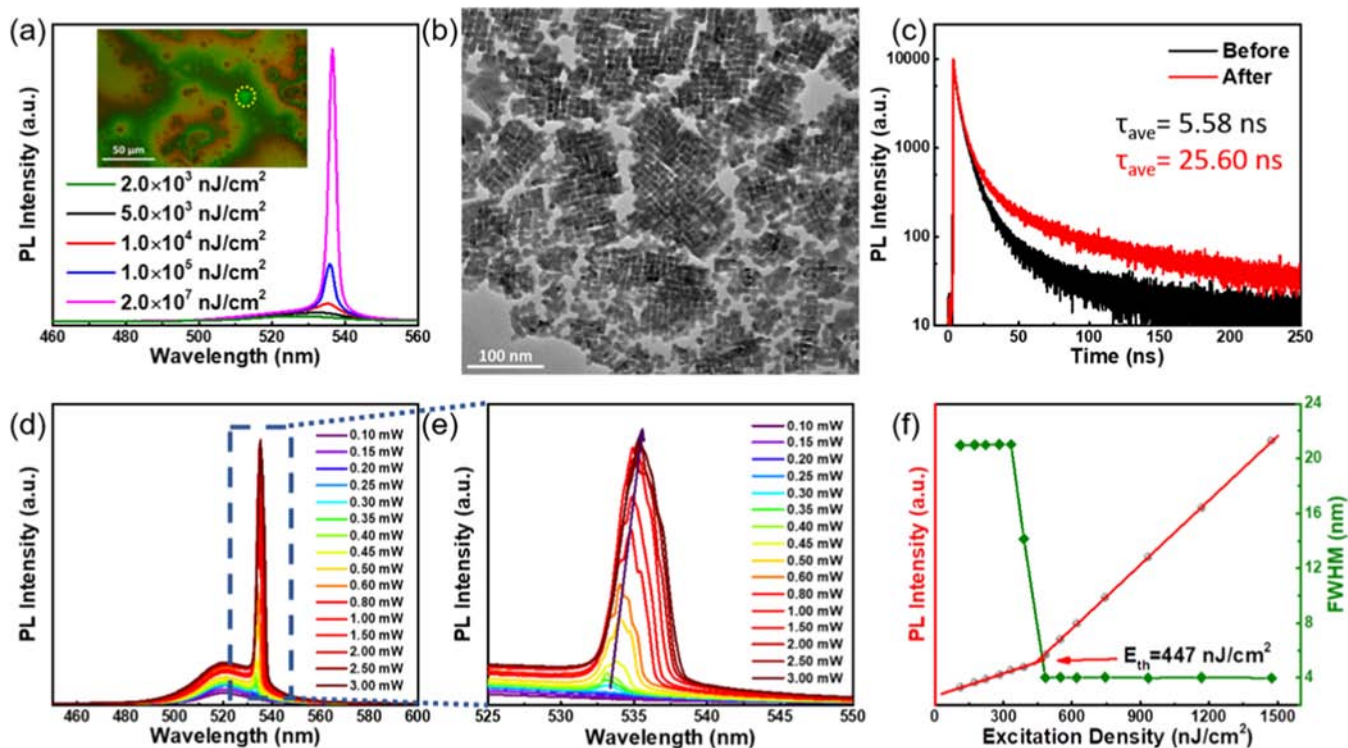
**Figure 4.** (a) Micro-PL spectra of the core−shell FAPbBr$_3$/CsPbBr$_3$ PeNCs at different excitation intensities. Inset is the image captured from an optical microscope, where the circle indicates the laser spot. (b) TEM image of the core−shell FAPbBr$_3$/CsPbBr$_3$ PeNCs after laser irradiation. (c) TRPL characterization of the core−shell FAPbBr$_3$/CsPbBr$_3$ PeNCs before and after laser irradiation. (d) Emission from the core−shell FAPbBr$_3$/CsPbBr$_3$ PeNCs at different pump fluences. (e) Details enlarged from (d). (f) The corresponding integrated intensity as a function of excitation density, where a threshold of $E_{th}$ = 447 $\mu$J/cm$^2$ for ASE can be determined.

band gap of CsPbBr$_3$ and FAPbBr$_3$,[48,49] the band diagram of the core−shell CsPbBr$_3$/FAPbBr$_3$ is calculated by DFT as a quasi-type II band alignment (Figure S4) and drawn in Figure 2f to discuss the mechanism. The band offset between the valence bands of CsPbBr$_3$ (VB$_{Cs}$) and FAPbBr$_3$ (VB$_{FA}$) is only 0.021 eV, which is similar to the energy difference between Peak 1 and Peak 2 at 50 K. For low excitation power (<2.5 mW), electrons in the conduction band of FAPbBr$_3$ (CB$_{FA}$) preferentially recombine with the holes in VB$_{Cs}$. Therefore, with the increase of excitation power, this recombination channel will dominate and lead to the decrease of $I_1/I_2$. For moderate excitation power (between 2.5 and 5.0 mW), the holes in VB$_{Cs}$ will gain enough energy from collision and be transferred to VB$_{FA}$, causing the emission of Peak 1. Therefore, with the increase of excitation power, the integrated PL intensity of Peak 1 increases sharply, which results in the increase of $I_1/I_2$. For high excitation power (> 5.0 mW), dynamic balance is reached and a constant ratio of $I_1/I_2$ can be observed. It is noted that the profile of the Peak 1 emission becomes symmetric at temperatures above 200 K. With the increase of temperature, the holes confined in VB$_{Cs}$ can gain enough thermal energy and be transferred to VB$_{FA}$, which contributes to the radiative recombination of Peak 1 and leads to the enhanced integrated PL intensity. In addition, the FWHM decreases at high temperatures due to the vanishing of Peak 2, which corresponds to the quasi-type II structure.[50,51]

The long-term stability of PeNCs is of paramount importance for their application in optoelectronic devices. Hence, the photostability measurement of FAPbBr$_3$ and core−shell FAPbBr$_3$/CsPbBr$_3$ PeNCs were performed. As depicted in Figure 3a, after exposure to 355 nm nanosecond laser for

1440 min, the PL intensity of FAPbBr$_3$ PeNCs attenuates up to 40%, while that of the core−shell PeNCs is attenuated only 10%. Moreover, the core−shell PeNCs show better spectral stability (Figure 3b). Therefore, it can be concluded that the photostability of core−shell PeNCs is significantly improved compared to that of bare FAPbBr$_3$ PeNCs. It is interesting that the clear signatures of ASE emission, including narrowing of the emission peaks and a steep rise in intensity above the threshold, appear in the core−shell PeNCs after laser irradiation for a period, as shown in Figure 3c. However, no gain was detected for core-only FAPbBr$_3$ PeNCs.

To discuss why ASE was only observed in the core−shell FAPbBr$_3$/CsPbBr$_3$ PeNCs, micro-PL measurement was carried out, and the result is shown in Figure 4a. The inset is the image of the core−shell PeNCs, and the yellow dashed circle marks the laser spot. It can be seen that there are flat surfaces and clusters (dark areas) on the film. ASE behavior can be observed on the flat surfaces, while only spontaneous emission can be detected for clusters, as shown in Figure S6c. Morphological characterization of FAPbBr$_3$ and core−shell FAPbBr$_3$/CsPbBr$_3$ PeNCs after laser irradiation was performed, and the corresponding TEM images are shown in Figures 4b and S7a, respectively. It was found that for FAPbBr$_3$ PeNCs, the morphology became uneven and the average size increased after laser irradiation. However, the size of the material remains unchanged for the core−shell FAPbBr$_3$/CsPbBr$_3$ PeNCs (Figure 4b). Furthermore, EDS images in Figure S7b,c display the element distribution of Cs$^+$ in the core−shell PeNCs. It can see that before and after laser irradiation, the distribution of Cs$^+$ hardly changes in the sample, which also supports the observation.

It is well-known that due to the ubiquitous ion migration, PeNCs undergo self-assembling behavior even in the absence of an external interference.[52−54] Meanwhile, the presence of surface defect states and laser-induced effect accelerates this ion migration process,[55−57] which results in the size increase of FAPbBr$_3$ PeNCs. This spontaneous behavior introduces more defect states,[58] which may be responsible for the absent ASE behavior in FAPbBr$_3$ PeNCs. In addition, it was proved that upon photoexcitation, organic cations diffuse out from the crystal edges and surface, causing the degradation of the inorganic layer.[59] This laser-induced degradation of PeNCs also hindered the generation of ASE in FAPbBr$_3$ PeNCs. In addition, it can also explain why the emission of FAPbBr$_3$ PeNCs decayed faster after being exposed to the nanosecond laser. In contrast, the outer layer of core−shell FAPbBr$_3$/CsPbBr$_3$ PeNCs is composed of an all-inorganic perovskite, which not only eliminates the diffusion of the organic group but also prevents the outward diffusion of organic cations in the core. It was demonstrated that the organic cation could assist defect migration through the charge redistribution along with the ionic motion, providing a local charge screening mechanism that may further speed up ion migration.[60] The A-site cation ($Cs^+$) in the outer layer of the core−shell PeNCs is less polar, less acidic, and less orientated than $FA^+$, which can efficiently prevent the ion migration. Therefore, after being exposed to the laser, the photon energy and intensity of the core−shell PeNCs can be maintained.

The PL decay of the core−shell FAPbBr$_3$/CsPbBr$_3$ PeNCs before and after laser irradiation was compared (Figure 4c), and the fitting results gave the averaged PL lifetime values of 5.58 and 25.60 ns, respectively. It is obvious that the treated core−shell PeNCs possess a longer PL lifetime, most likely owing to the passivation of defect states by laser irradiation.[61−63] It is reported that ultraviolet (UV) light irradiation can effectively passivate both the shallow level and deep level defect states.[64] However, their passivation mechanism is different. The passivation of shallow level defect states is the dissociation of the adsorbed hydroxyl groups, while the passivation of deep level defect states is the dissociation of adsorbed water molecules. For the core−shell FAPbBr$_3$/CsPbBr$_3$ PeNCs discussed herein, defects in the interface are the main ones. Taking into account the coating of the shell layer and the ionic nature of CsPbBr$_3$, the number of water molecules that can be adsorbed by the interface defects is much smaller than that of the hydroxyl group. Under UV laser (355 nm) irradiation, the hydroxyl groups dissociate and the defects are passivated, leading to the appearance of ASE. Therefore, it is concluded that improvement is due to the UV light passivation of shallow level defect states. Moreover, it was known that defects at the interface as a nonradiative recombination center may be passivated by the microwave treatment method.[65] Therefore, to confirm this hypothesis, the as-grown core−shell PeNCs were treated with microwaves. As shown in Figure S8, the emission property of the core−shell PeNCs is closely related to the microwave treatment. The longer the treated time, the earlier the observation of the ASE behavior. In addition, the emission intensity of the core−shell PeNCs after microwave treatment was enhanced by about 4 times. This dramatic increase in the PL intensity indicates that defect states mainly originate from the interface between the core and the shell. It should be noted that although the ASE behavior can be observed without laser irradiation after sufficient microwave treatment (5 min), the intensity of ASE is lower than that of the sample with 3 min microwave treatment. This may be attributed to the decomposition of the inner core due to the heat generated by excessive microwaves. Compared with core−shell FAPbBr$_3$/CsPbBr$_3$ PeNCs, there is still no ASE behavior in bare FAPbBr$_3$ PeNCs (Figure S9). The reason can be ascribed to the ion migration in FAPbBr$_3$ PeNCs due to the absence of the shell. This ion migration process leads to an increase in the size, which, in turn, introduces new defects, resulting in no ASE behavior.

Figure 4d shows the ASE behavior of the core−shell PeNCs without the microwave treatment, which possesses an ultranarrow FWHM of around 3.1 nm and is red shifted by around 15 nm with respect to the spontaneous emission. Figure 4e shows the details in Figure 4d, and the red-shift of the ASE may originate from reabsorption during single exciton lasing.[66] The threshold for building ASE is 447 nJ/cm$^2$ for the core−shell FAPbBr$_3$/CsPbBr$_3$ PeNCs (Figure 4f). These results indicate that the core−shell FAPbBr$_3$/CsPbBr$_3$ PeNCs can act as an excellent gain medium for high-performance lasers for optoelectronic applications.

## ■ CONCLUSIONS

In retrospect, the emission characteristics of bare FAPbBr$_3$ and the core−shell FAPbBr$_3$/CsPbBr$_3$ PeNCs are studied using power- and temperature-dependent laser spectroscopy. The electronic structure of the core−shell FAPbBr$_3$/CsPbBr$_3$ PeNCs is determined to be quasi-type II band alignment. In addition, compared with FAPbBr$_3$, the core−shell FAPbBr$_3$/CsPbBr$_3$ PeNCs exhibit better photostability under 355 nm nanosecond laser irradiation. The integrated PL intensity attenuates by only ∼10% and the photon energy remains identical, which benefits from the suppression of ion migration. Interestingly, the ASE behavior with a threshold of 447 nJ/cm$^2$ was observed in the core−shell PeNCs, which can be ascribed to the laser irradiation-induced interface defect passivation. This work would provide new opportunities for the design and utilization of the core−shell PeNCs in optoelectronic devices.

## ■ ASSOCIATED CONTENT

### ⓢ Supporting Information

The Supporting Information is available free of charge at https://pubs.acs.org/doi/10.1021/acsami.1c18025.

> Figure S1: details from temperature-dependent PL spectroscopy; Figures S2 and S3: power-dependent PL of FAPbBr$_3$ PeNCs and core−shell PeNCs at 50 and 295 K; Figure S4: DFT calculation of the band structures; Figure S5: PL emission of the core−shell PeNCs with different concentrations; Figure S6: images captured by optical microscopy; Figure S7: TEM images before and after laser irradiation; Figures S8 and S9: PL of the core−shell PeNCs and bare-core PeNCs with different microwave treated times. The raw/processed data required to reproduce these findings cannot be shared at this time due to technical or time limitations. (PDF)

## ■ AUTHOR INFORMATION

### Corresponding Authors

Tingchao He − College of Physics and Optoelectronic Engineering, Shenzhen University, Shenzhen 518060, China; ⓞ orcid.org/0000-0003-1040-0596; Email: tche@szu.edu.cn

**Rui Chen** − *Department of Electrical and Electronic Engineering, Southern University of Science and Technology, Shenzhen 518055, China;* orcid.org/0000-0002-0445-7847; Email: chenr@sustech.edu.cn

**Authors**

**Xuanyu Zhang** − *Department of Electrical and Electronic Engineering, Southern University of Science and Technology, Shenzhen 518055, China*

**Zhihang Guo** − *College of Physics and Optoelectronic Engineering, Shenzhen University, Shenzhen 518060, China*

**Ruxue Li** − *Department of Electrical and Electronic Engineering, Southern University of Science and Technology, Shenzhen 518055, China; School of Electrical and Information Engineering, Guangxi University of Science and Technology, Liuzhou 545006 Guangxi, China*

**Jiahao Yu** − *Department of Electrical and Electronic Engineering, Southern University of Science and Technology, Shenzhen 518055, China*

**Baozhen Yuan** − *Department of Electrical and Electronic Engineering, Southern University of Science and Technology, Shenzhen 518055, China*

**Baian Chen** − *Department of Electrical and Electronic Engineering, Southern University of Science and Technology, Shenzhen 518055, China; Department of Applied Biology and Chemical Technology, The Hong Kong Polytechnic University, Kowloon 999077 Hong Kong SAR, China*

Complete contact information is available at:
https://pubs.acs.org/10.1021/acsami.1c18025

**Author Contributions**

The manuscript was written through contributions of all authors. All authors have given approval to the final version of the manuscript.

**Notes**

The authors declare no competing financial interest.

## ACKNOWLEDGMENTS

## REFERENCES

(1) Tan, Z.-K.; Moghaddam, R.; Lai, M.; Docampo, P.; Higler, R.; Deschler, F.; Price, M.; Sadhanala, A.; Pazos, L.; Credgington, D.; Hanusch, F.; Bein, T.; Snaith, H.; Friend, R. Bright Light-Emitting Diodes Based on Organometal Halide Perovskite. *Nat. Nanotechnol.* **2014**, *9*, 687−692.

(2) Yang, X.; Zhang, X.; Deng, J.; Chu, Z.; Jiang, Q.; Meng, J.; Wang, P.; Zhang, L.; Yin, Z.; You, J. Efficient Green Light-Emitting Diodes Based on Quasi-Two-Dimensional Composition and Phase Engineered Perovskite with Surface Passivation. *Nat. Commun.* **2018**, *9*, No. 570.

(3) Hoye, R.; Chua, M.; Musselman, K.; Li, G.; Lai, M.-L.; Tan, Z.-K.; Greenham, N.; MacManus-Driscoll, J.; Friend, R.; Credgington, D. Enhanced Performance in Fluorene-Free Organometal Halide Perov-skite Light-Emitting Diodes Using Tunable, Low Electron Affinity Oxide Electron Injectors. *Adv. Mater.* **2015**, *27*, 1414−1419.

(4) Filip, M.; Eperon, G.; Snaith, H.; Giustino, F. Steric Engineering of Metal-Halide Perovskites with Tunable Optical Band Gaps. *Nat. Commun.* **2014**, *5*, No. 5757.

(5) Wang, S.; Yu, J.; Zhang, M.; Chen, D.; Li, C.; Chen, R.; Jia, G.; Rogach, A.; Yang, X. Stable, Strongly Emitting Cesium Lead Bromide Perovskite Nanorods with High Optical Gain Enabled by an Intermediate Monomer Reservoir Synthetic Strategy. *Nano Lett.* **2019**, *19*, 6315−6322.

(6) Al-Ashouri, A.; Köhnen, E.; Li, B.; Magomedov, A.; Hempel, H.; Caprioglio, P.; Márquez, J.; Viches, A.; Kasparavicius, E.; Smith, J.; Phung, N.; Menzel, D.; Grischek, M.; Kegelmann, L.; Skroblin, D.; Gollwitzer, C.; Malinauskas, T.; Jošt, M.; Matič, G.; Rech, B.; Schlatmann, R.; Topič, M.; Korte, L.; Abate, A.; Stannowski, B.; Neher, D.; Stolterfoht, M.; Unold, T.; Getautis, V.; Albrecht, S. Monolithic Perovskite/Silicon Tandem Solar Cell with> 29% Efficiency by Enhanced Hole Extraction. *Science* **2020**, *370*, 1300−1309.

(7) Lin, K.; Xing, J.; Quan, L.; Arquer, F.; Gong, X.; Lu, J.; Xie, L.; Zhao, W.; Zhang, D.; Yan, C.; Li, W.; Liu, X.; Lu, Y.; Kirman, J.; Sargent, E.; Xiong, Q.; Wei, Z. Perovskite Light-Emitting Diodes with External Quantum Efficiency Exceeding 20 Percent. *Nature* **2018**, *562*, 245−248.

(8) Zhang, Q.; Shang, Q.; Su, R.; Thu Ha Do, T.; Xiong, Q. Halide Perovskite Semiconductor Lasers: Materials, Cavity Design, and Low Threshold. *Nano Lett.* **2021**, *21*, 1903−1914.

(9) Dutta, J.; Ajith, M.; Dutta, S.; Kadhane, U.; Kochupurackal, B. J.; Rai, B. An Inherent Instability Study Using *ab* Initio Computational Methods and Experimental Validation of Pb(SCN)₂ Based Perov-skites for Solar Cell Applications. *Sci. Rep.* **2020**, *10*, No. 15241.

(10) Li, B.; Li, Y.; Zheng, C.; Gao, D.; Huang, W. Advancements in the Stability of Perovskite Solar Cells: Degradation Mechanisms and Improvement Approaches. *RSC Adv.* **2016**, *6*, 38079−38091.

(11) Conings, B.; Drijkoningen, J.; Gauquelin, N.; Babayigit, A.; D'Haen, J.; D'Olieslaeger, L.; Ethirajan, A.; Verbeeck, J.; Manca, J.; Mosconi, E.; De Angelis, F.; Boyen, H.-G. Intrinsic Thermal Instability of Methylammonium Lead Trihalide Perovskite. *Adv. Energy Mater.* **2015**, *5*, No. 1500477.

(12) De Roo, J.; Ibáñez, M.; Geiregat, P.; Nedelcu, G.; Walravens, W.; Maes, J.; Martins, J.; Van Driessche, I.; Kovalenko, M.; Hens, Z. Highly Dynamic Ligand Binding and Light Absorption Coefficient of Cesium Lead Bromide Perovskite Nanocrystals. *ACS Nano* **2016**, *10*, 2071−2081.

(13) Huang, S.; Li, Z.; Wang, B.; Zhu, N.; Zhang, C.; Kong, L.; Zhang, Q.; Shan, A.; Li, L. Morphology Evolution and Degradation of CsPbBr₃ Nanocrystals under Blue Light-Emitting Diode Illumination. *ACS Appl. Mater. Interfaces* **2017**, *9*, 7249−7258.

(14) Gottesman, R.; Gouda, L.; Kalanoor, B.; Haltzi, E.; Tirosh, S.; Rosh-Hodesh, E.; Tischler, Y.; Zaban, A.; Quarti, C.; Mosconi, E.; De Angelis, F. Photoinduced Reversible Structural Transformations in Free-Standing CH₃NH₃PbI₃ Perovskite Films. *J. Phys. Chem. Lett.* **2015**, *6*, 2332−2338.

(15) Udayabhaskararao, T.; Kazes, M.; Houben, L.; Lin, H.; Oron, D. Nucleation, Growth, and Structural Transformations of Perovskite Nanocrystals. *Chem. Mater.* **2017**, *29*, 1302−1308.

(16) Han, H.; Jeong, B.; Park, T.; Cha, W.; Cho, S.; Kim, Y.; Kim, H.; Kim, D.; Ryu, D.; Choi, W.; Park, C. Perovskite Nanopatterning: Highly Photoluminescent and Environmentally Stable Perovskite Nanocrystals Templated in Thin Self-Assembled Block Copolymer Films. *Adv. Funct. Mater.* **2019**, *29*, No. 1808193.

(17) Zhang, C.; Turyanska, L.; Cao, H.; Zhao, L.; Fay, M.; Temperton, R.; O'Shea, J.; Thomas, N.; Wang, K.; Luan, W.; Patanè, A. Hybrid Light Emitting Diodes Based on Stable, High Brightness All-Inorganic CsPbI₃ Perovskite Nanocrystals and InGaN. *Nanoscale* **2019**, *11*, 13450−13457.

(18) Sun, C.; Zhang, Y.; Ruan, C.; Yin, C.; Wang, X.; Wang, Y.; Yu, W. Efficient and Stable White LEDs with Silica-Coated Inorganic Perovskite Quantum Dots. *Adv. Mater.* **2016**, *28*, 10088−10094.

(19) Li, R.; Li, B.; Fang, X.; Wang, D.; Shi, Y.; Liu, X.; Chen, R.; Wei, Z. Self-Structural Healing of Encapsulated Perovskite Micro-crystals for Improved Optical and Thermal Stability. *Adv. Mater.* **2021**, *33*, No. 2100466.

(20) Raja, S.; Bekenstein, Y.; Koc, M.; Fischer, S.; Zhang, D.; Lin, L.; Ritchie, R.; Yang, P.; Yehonadav, P. Encapsulation of Perovskite Nanocrystals into Macroscale Polymer Matrices: Enhanced Stability and Polarization. *ACS Appl. Mater. Interfaces* **2016**, *8*, 35523−35533.

(21) Li, Z.; Hofman, E.; Li, J.; Davis, A.; Tung, C.-H.; Wu, L.-Z.; Zheng, W. Photoelectrochemically Active and Environmentally Stable $CsPbBr_3/TiO_2$ Core/Shell Nanocrystals. *Adv. Funct. Mater.* **2018**, *28*, No. 1704288.

(22) Bhaumik, S.; Veldhuis, S.; Fong Ng, Y.; Li, M.; Muduli, S.; Sum, T.; Damodaran, B.; Mhaisalkar, S.; Mathews, N. Highly Stable, Luminescent Core-Shell Type Methylammonium-Octylammonium Lead Bromide Layered Perovskite Nanoparticles. *Chem. Commun.* **2016**, *52*, 7118−7121.

(23) Chen, W.; Bhaumik, S.; Veldhuis, S.; Xing, G.; Xu, Q.; Grätzel, M.; Mhaisalkar, S.; Mathews, N.; Sum, T. Giant Five-Photon Absorption from Multidimensional Core-Shell Halide Perovskite Colloidal Nanocrystals. *Nat. Commun.* **2017**, *8*, No. 15198.

(24) Chen, X.; Lou, Y.; Samia, A.; Burda, C. Coherency Strain Effects on the Optical Response of Core/Shell Heteronanostructures. *Nano Lett.* **2003**, *3*, 799−803.

(25) Smith, A.; Mohs, A.; Nie, S. Tuning the Optical and Electronic Properties of Colloidal Nanocrystals by Lattice Strain. *Nat. Nano-technol.* **2009**, *4*, 56−63.

(26) Yu, D.; Cao, F.; Gao, Y.; Xiong, Y.; Zeng, H. Room-Temperature Ion-Exchange-Mediated Self-Assembly toward Forma-midinium Perovskite Nanoplates with Finely Tunable, Ultrapure Green Emissions for Achieving Rec. 2020 Displays. *Adv. Funct. Mater.* **2018**, *28*, No. 1800248.

(27) Wang, J.; Song, C.; He, Z.; Mai, C.; Xie, G.; Mu, L.; Cun, Y.; Li, J.; Wang, J.; Peng, J.; Cao, Y. All-Solution-Processed Pure Formamidinium-Based Perovskite Light-Emitting Diodes. *Adv. Mater.* **2018**, *30*, No. 1804137.

(28) Zhang, C.; Wang, S.; Li, X.; Yuan, M.; Turyanska, L.; Yang, X. Core/Shell Perovskite Nanocrystals: Synthesis of Highly Efficient and Environmentally Stable $FAPbBr_3/CsPbBr_3$ for LED Applications. *Adv. Funct. Mater.* **2020**, *30*, No. 1910582.

(29) Segall, M.; Lindan, P.; Probert, M.; Pickard, C.; Hasnip, P.; Clark, S.; Payne, M. First-Principles Simulation: Ideas, Illustrations and the CASTEP Code. *J. Phys.: Condens. Matter* **2002**, *14*, 2717−2744.

(30) Jain, A.; Ong, S.; Hautier, G.; Chen, W.; Richards, W.; Dacek, S.; Cholia, S.; Gunter, D.; Skinner, D.; Ceder, G.; Persson, K. Commentary: The Materials Project: A Materials Genome Approach to Accelerating Materials Innovation. *APL Mater.* **2013**, *1*, No. 011002.

(31) Perdew, J.; Burke, K.; Ernzerhof, M. Generalized Gradient Approximation Made Simple. *Phys. Rev. Lett.* **1996**, *77*, 3865−3868.

(32) Fischer, T.; Almlof, J. General Methods for Geometry and Wave Function Optimization. *J. Phys. Chem. A* **1992**, *96*, 9768−9774.

(33) Monkhorst, H.; Pack, J. Special Points for Brillouin-Zone Integrations. *Phys. Rev. B* **1976**, *13*, 5188−5192.

(34) Polavarapu, L.; Nickel, B.; Feldmann, J.; Urban, A. Advances in Quantum-Confined Perovskite Nanocrystals for Optoelectronics. *Adv. Energy Mater.* **2017**, *7*, No. 1700267.

(35) Yang, L.; Wei, K.; Xu, Z.; Li, F.; Chen, R.; Zheng, X.; Cheng, X.; Jiang, T. Nonlinear Absorption and Temperature-Dependent Fluorescence of Perovskite $FAPbBr_3$ Nanocrystal. *Opt. Lett.* **2018**, *43*, 122−125.

(36) Keshavarz, M.; Ottesen, M.; Wiedmann, S.; Wharmby, M.; Küchler, R.; Yuan, H.; Debroye, E.; Steele, J.; Martens, J.; Hussey, N.; Bremholm, M.; Roeffaers, M.; Hofkens, J. Tracking Structural Phase Transitions in Lead-Halide Perovskites by Means of Thermal Expansion. *Adv. Mater.* **2019**, *8*, No. 1900521.

(37) Wang, X.; Wang, Q.; Chai, Z.; Wu, W. The Thermal Stability of $FAPbBr_3$ Nanocrystals from Temperature-Dependent Photolumines-cence and First-Principles Calculations. *RSC Adv.* **2020**, *10*, 44373−44381.

(38) Li, D.; Wang, G.; Cheng, H. C.; Chen, C. Y.; Wu, H.; Liu, Y.; Huang, Y.; Duan, X. Size-Dependent Phase Transition in Methyl-ammonium Lead Iodide Perovskite Microplate Crystals. *Nat. Commun.* **2016**, *7*, No. 11330.

(39) Lee, K. J.; Turedi, B.; Giugni, A.; Lintangpradipto, M. N.; Zhumekenov, A. A.; Alsalloum, A. Y.; Min, J.-H.; Dursun, I.; Naphade, R.; Mitra, S.; Roqan, I. S.; Ooi, B. S.; Mohammed, O. F.; Di Fabrizio, E.; Cho, N.; Bakr, O. M. Domain-Size-Dependent Residual Stress Governs the Phase-Transition and Photoluminescence Behavior of Methylammonium Lead Iodide. *Adv. Funct. Mater.* **2021**, *31*, No. 2008088.

(40) Zhang, X.; Pang, G.; Xing, G.; Chen, R. Temperature Dependent Optical Characteristics of All-Inorganic $CsPbBr_3$ Nano-crystals Film. *Mater. Today Phys.* **2020**, *15*, No. 100259.

(41) Schueller, E.; Laurita, G.; Fabini, D.; Stoumpos, C.; Kanatzidis, M.; Seshadri, R. Crystal Structure Evolution and Notable Thermal Expansion in Hybrid Perovskites Formamidinium Tin Iodide and Formamidinium Lead Bromide. *Inorg. Chem.* **2018**, *57*, 695−701.

(42) Lei, X.; Yu, K. First-Principles Calculations on Strain and Electric Field Induced Band Modulation and Phase Transition of Bilayer $WSe_2MoS_2$ Heterostructure. *Physica E* **2018**, *98*, 17−22.

(43) Glinchuk, M.; Eliseev, E.; Morozovska, A. Influence of Built-In Internal Electric Field on Ferroelectric Film Properties and Phase Diagram. *Ferroelectrics* **2007**, *354*, 86−98.

(44) Schmidt, T.; Lischka, K.; Zulehner, W. Excitation-Power Dependence of the Near-Band-Edge Photoluminescence of Semi-conductors. *Phys. Rev. B* **1992**, *45*, No. 8989.

(45) Kondo, T.; Azuma, T.; Yuasa, T.; Ito, R. Biexciton Lasing in the Layered Perovskite-Type Material $(C_6H_{13}NH_3)_2PbI_4$. *Solid State Commun.* **1998**, *105*, 253−255.

(46) Kunugita, H.; Kiyota, Y.; Udagawa, Y.; Takeoka, Y.; Nakamura, Y.; Sano, J.; Matsushita, T.; Kondo, T.; Ema, K. Exciton-Exciton Scattering in Perovskite $CH_3NH_3PbBr_3$ Single Crystal. *Jpn. J. Appl. Phys.* **2016**, *55*, No. 060304.

(47) Galkowski, K.; Mitioglu, A.; Miyata, A.; Plochocka, P.; Portugall, O.; Eperon, G.; Wang, J.; Stergiopoulos, T.; Stranks, S.; Snaith, H.; Nicholas, R. Determination of the Exciton Binding Energy and Effective Masses for Methylammonium and Formamidinium Lead Tri-Halide Perovskite Semiconductors. *Energy Environ. Sci.* **2016**, *9*, 962−970.

(48) Tong, G.; Chen, T.; Li, H.; Qiu, L.; Liu, Z.; Dang, Y.; Song, W.; Ono, L.; Jiang, Y.; Qi, Y. Phase Transition Induced Recrystallization and Low Surface Potential Barrier Leading to 10.91%-Efficient $CsPbBr_3$ Perovskite Solar Cells. *Nano Energy* **2019**, *65*, No. 104015.

(49) Hanusch, F.; Wiesenmayer, E.; Mankel, E.; Binek, A.; Angloher, P.; Fraunhofer, C.; Giesbrecht, N.; Feckl, J.; Jaegermann, W.; Johrendt, D.; Bein, T.; Docampo, P. Efficient Planar Heterojunction Perovskite Solar Cells Based on Formamidinium Lead Bromide. *J. Phys. Chem. Lett.* **2014**, *5*, 2791−2795.

(50) Wen, X.; Sitt, A.; Yu, P.; Toh, Y.; Tang, J. Temperature Dependent Spectral Properties of Type-I and Quasi Type-II CdSe/CdS Dot-In-Rod Nanocrystals. *Phys. Chem. Chem. Phys.* **2012**, *14*, 3505−3512.

(51) Li, H.; Tang, J.; Kang, Y.; Zhao, H.; Fang, D.; Fang, X.; Chen, R.; Wei, Z. Optical Properties of Quasi-Type-II Structure in GaAs/GaAsSb/GaAs Coaxial Single Quantum-Well Nanowires. *Appl. Phys. Lett.* **2018**, *113*, No. 233104.

(52) Aharon, S.; Layani, M.; Cohen, B.; Shukrun, E.; Magdassi, S.; Etgar, L. Self-Assembly of Perovskite for Fabrication of Semi-transparent Perovskite Solar Cells. *Adv. Mater. Interfaces* **2015**, *2*, No. 1500118.

(53) Tong, Y.; Yao, E.; Manzi, A.; Bladt, E.; Wang, K.; Döblinger, M.; Bals, S.; Müller-Buschbaum, P.; Urban, A.; Polavarapu, L.; Feldmann, J. Spontaneous Self-Assembly of Perovskite Nanocrystals into Electronically Coupled Supercrystals: Toward Filling the Green Gap. *Adv. Mater.* **2018**, *30*, No. 1801117.

(54) Liu, Y.; Siron, M.; Lu, D.; Yang, J.; dos Reis, R.; Cui, F.; Gao, M.; Lai, M.; Lin, J.; Kong, Q.; Lei, T.; Kang, J.; Jin, J.; Ciston, J.; Yang, P. Self-Assembly of Two-Dimensional Perovskite Nanosheet Building Blocks into Ordered Ruddlesden-Popper Perovskite Phase. *J. Am. Chem. Soc.* **2019**, *141*, 13028−13032.

(55) Wang, Y.; Li, X.; Sreejith, S.; Cao, F.; Wang, Z.; Stuparu, M.; Zeng, H.; Sun, H. Photon Driven Transformation of Cesium Lead Halide Perovskites from Few-Monolayer Nanoplatelets to Bulk Phase. *Adv. Mater.* **2016**, *28*, 10637−10643.

(56) Gardiner, G.; Islam, M. Anti-Site Defects and Ion Migration in the $LiFe_{0.5}Mn_{0.5}PO_4$ Mixed-Metal Cathode Material. *Chem. Mater.* **2010**, *22*, 1242−1248.

(57) Meggiolaro, D.; Mosconi, E.; De Angelis, F. Formation of Surface Defects Dominates Ion Migration in Lead-Halide Perovskites. *ACS Energy Lett.* **2019**, *4*, 779−785.

(58) Guo, X.; Zhang, Z. Grain Size Dependent Grain Boundary Defect Structure: Case of Doped Zirconia. *Acta Mater.* **2003**, *51*, 2539−2547.

(59) Fang, H.; Yang, J.; Tao, S.; Adjokatse, S.; Kamminga, M.; Ye, J.; Blake, G.; Even, J.; Antonietta Loi, M. Unravelling Light-Induced Degradation of Layered Perovskite Crystals and Design of Efficient Encapsulation for Improved Photostability. *Adv. Funct. Mater.* **2018**, *28*, No. 1800305.

(60) Mosconi, E.; De Angelis, F. Mobile Ions in Organohalide Perovskites: Interplay of Electronic Structure and Dynamics. *ACS Energy Lett.* **2016**, *1*, 182−188.

(61) Ardekani, H.; Younts, R.; Yu, Y.; Cao, L.; Gundogdu, K. Reversible Photoluminescence Tuning by Defect Passivation via Laser Irradiation on Aged Monolayer $MoS_2$. *ACS Appl. Mater. Interfaces* **2019**, *11*, 38240−38246.

(62) Rao, R.; Carozo, V.; Wang, Y.; Islam, A.; Perea-Lopez, N.; Fujisawa, K.; Crespi, V.; Terrones, M.; Maruyama, B. Dynamics of Cleaning, Passivating and Doping Monolayer $MoS_2$ by Controlled Laser Irradiation. *2D Mater.* **2019**, *6*, No. 045031.

(63) Fang, H.; Wang, F.; Adjokatse, S.; Zhao, N.; Antonietta Loi, M. Photoluminescence Enhancement in Formamidinium Lead Iodide Thin Films. *Adv. Funct. Mater.* **2016**, *26*, 4653−4659.

(64) Roghabadi, F. A.; Fumani, N. M. R.; Alidaei, M.; Ahmadi, V.; Sadrameli, S. M. High Power UV-Light Irradiation as a New Method for Defect Passivation in Degraded Perovskite Solar Cells to Recover and Enhance the Performance. *Sci. Rep.* **2019**, *9*, No. 9448.

(65) Chen, Q.; Ma, T.; Wang, F.; Liu, Y.; Liu, S.; Wang, J.; Cheng, Z.; Chang, Q.; Yang, R.; Huang, W.; Wang, L.; Qin, T.; Huang, W. Rapid Microwave-Annealing Process of Hybrid Perovskites to Eliminate Miscellaneous Phase for High Performance Photovoltaics. *Adv. Sci.* **2020**, *7*, No. 2000480.

(66) Yakunin, S.; Protesescu, L.; Krieg, F.; Bodnarchuk, M.; Nedelcu, G.; Humer, M.; De Luca, G.; Fiebig, M.; Heiss, W.; Kovalenko, M. Low-Threshold Amplified Spontaneous Emission and Lasing from Colloidal Nanocrystals of Caesium Lead Halide Perovskites. *Nat. Commun.* **2015**, *6*, No. 8056.